ADVANCED MATERIALS
www.advmat.de

Unlock the Potassium Storage Behavior of Single-Phased Tungsten Selenide Nanorods via Large Cation Insertion

*Zhongchen Zhao, Tian Xu, and Xuebin Yu**

Metal chalcogenide anodes with a layered structure have been regarded as potential K-based electrochemical energy storage devices with high energy density for large-scale energy storage applications. However, their development is impeded by the slow K-ion transport kinetics and poor structural stability. In this work, the energy-storage behavior is investigated first and decisively associated them with the capacity-degradation of the promising layer-structured WSe_2 from an integrated chemical and physical point of view. Then, a single-phased WSe_2 with pre-intercalated high K content (SP-K_xWSe_2) is designed to overcome the capacity-degradation issue fundamentally. Theoretical calculations clarify the beneficial effect of K-ions inside the interlayer of WSe_2 on boosting its electrochemical performance, including increasing the electronic conductivity, promoting the K-ion diffusivity, and improving the structural stability. The novel design enables the K-ions pre-intercalated WSe_2 anode material to exhibit a high reversible specific capacity of 211 mAh g^{-1} at 5 A g^{-1} and superior cycling stability (89.3% capacity retention after 5000 cycles at 1 A g^{-1}). Especially, the K-ion hybrid capacitor, assembled from the anode of SP-K_xWSe_2 and the cathode of porous activated carbon, delivers superior energy-density up to 175 Wh kg^{-1}, high power-density as well as exceptional cycling stability.

1. Introduction

Grid electrochemical energy storage systems capable of more energy are essential for the integration of intermittent green energy into smart grid. Among various energy storage devices, high-energy rechargeable batteries consisting of alkali ion (Li, Na, and K) (de)intercalation are receiving considerable attention, among which the potassium ion (K) based devices demonstrate superiority owing to the higher abundance, and lower standard redox potential (–2.93 V versus standard hydrogen electrode) than that of its Li and Na counterpart.[1–5] Moreover, superior rate capability of K-based electrochemical energy storage (KEES) device is projected, owing to the much higher ionic conductivity of K-ion based electrolyte derived from the small Stokes radius of solvated K. However, the advancement of KEES was severely hindered by the lack of suitable anodes that can endure the structure degradation during the reversible insertion of large size of K-ions (1.38 Å).[6–9] So far, various electrode materials, such as carbonaceous materials, K-alloying materials, metal oxides, and MXene, have been studied widely as battery-type anodes.[10–12] However, the research of KEESs is still in its early stages, and the development of suitable anode materials with high-rate capability still remains a great challenge.[13–15]

2D layered transition metal dichalcogenides (2D TMDs), including sulfides (e.g., MoS_2, VS_2, and ReS_2) and selenides (e.g., $MoSe_2$, VSe_2, and $NbSe_2$), have attracted attention as anode materials for K-ion batteries owing to their high theoretical capacities and tunable interlayer spacing.[16,17] Among the 2D TMDs, tungsten selenium (WSe_2) exhibits several attractive features for high-capacity and high-rate K storage.[18,19] The relatively large interlayer spacing of 0.678 nm for its (002) plane affords advantages for the (de) insertion of K^+ and the volume change during repeated cycling. Compared with Li^+ and Na^+ (>1.5 V), the relatively low potential plateau of the electrochemical K-(de)intercalation into WSe_2 (<1.0 V) is beneficial for the high working voltage of full cells, thereby improving the energy density of KEESs.[20,21] During the past several years, several precious works involved in the improvement of WSe_2-based electrodes were mainly focused on constructing reasonable nanostructure and carbon coating.[18–20] However, evident structural distortion derived from the large K-ion inserted in these electrodes is still inevitable, particularly after long cycles, resulting in drastically decayed cycling performance. In addition, the sluggish K-ion diffusion in WSe_2 due to the limited interlayer space causes poor rate capability, suggesting that the accommodation of the bulky K^+ is less favorable than Li^+ and Na^+ in such compact layered structures.

Clearly, the expansion and improvement of these studies on K-ion storage remain to be promoted, which is crucial in determining whether the KEES goals of high reversible capacity, superior rate capability, and favorable cycling stability can be achieved for WSe_2 materials. Previous research has demonstrated that large cations such as K^+, NH_4^+, and polyaniline can be inserted into lattice during the synthesis process of 2D TMDs, layered oxides, oxyhydroxides, and olivines, resulting in increased electrochemically active surface area, lattice spacing

Z. Zhao, T. Xu, X. Yu
Department of Materials Science
Fudan University
Shanghai 200433, P. R. China
E-mail: yuxuebin@fudan.edu.cn

The ORCID identification number(s) for the author(s) of this article can be found under https://doi.org/10.1002/adma.202208096.

DOI: 10.1002/adma.202208096

and improved electrocatalysis towards the conversion reaction.[22–25] The guest cations, which partially occupied the available site at the surface of the host lattice, are expected to act synergistically with charge carriers (Li^+, Na^+, and Mg^{2+}) and affect the reversible charge storage characteristic of host. Therefore, in theory, the insertion of suitable large cations into WSe_2 lattice is capable to achieve large reversible capacity and enhanced cycling stability with a reinforced layered structure. However, the adoption of "pre-intercalation" strategy for WSe_2 has not yet been demonstrated as promising anode material for KEESs.

In this work, combined experimental measurements with theoretical calculations, the electrochemical mechanism responsible for the decrease of capacity of WSe_2 anode materials was first figured out, which is closely bound up with the dissolution of W and Se species, and the collapse of WSe_2. At this point, we have carried out a comprehensive study on the role of the successfully pre-intercalated K-ions in improving the electrochemical activities of electrode materials by focusing on pre-intercalating K-ions in well-designed single-phased WSe_2 nanorod bundles (SP-WSe_2). The prepared single-phased K-ions intercalated WSe_2 nanorod bundles (SP-K_xWSe_2) demonstrate fast kinetics during reversible intercalation of K-ions, enabling it high-rate capability (211 mAh g^{-1} at 5 A g^{-1}) and long cycling life (89.3% capacity retention over 5000 cycles). Moreover, it can impart outstanding performance to K-ion hybrid capacitors (KIHCs), which affords a high energy density (175 Wh kg^{-1} at 250 W kg^{-1}) and a 94.8% capacity retention over 8500 cycles at 2000 W kg^{-1}. Our work provides experimentalists with executable optimizations corresponding to mismatched electrochemical behavior of their electrode materials, and new rational solutions for comprehending the carrier storage chemistry within electrodes.

2. Results and Discussion

2.1. Structure and Performance of Designed Anode

We present a facile two-step, high-yield strategy for efficient synthesis of the SP-WSe_2 from a single-source precursor. First, a certain amount of sodium tungstate and dilute nitric acid was dissolved into deionized water to form a transparent solution. It is notable that sodium tungstate will decompose into WO_{3-x} under a specific acidic environment (pH = 2.1) in hydrothermal process.[26] After high-energy crystallization processed at 190 °C in a sealed Teflon-lined reactor, WO_{3-x} self-assembles along a specific crystalline phase to form the WO_x nanorod structures. Finally, SP-WSe_2 was collected via selenization of WO_x in the nanorod matrix at an appropriate temperature, and the more detailed synthesis strategy is shown in the Experiment Methods (Supporting Information). The detailed microstructure and size of the product were identified by field-emission scanning electron microscopy (FESEM) and transmission electron microscopy (TEM) (**Figure 1**a–c and Figure S1, Supporting Information). The monodisperse SP-WSe_2 consisted of well-defined nanorods, varying in diameter between 5 and 10 µm depending on the number of polymerized nanorods (Figure 1a,b and Figure S1, Supporting Information). Figure 1c reproduces the selected area electron diffraction (SAED), which indicates the single and highly crystalline nature of the nanorods, and the clearly indexed (100), (102) facets confirm the orientation of the lattice with [010] along the axis of the nanorod. The microstructure was gained from X-ray diffraction (XRD) and top-view high-angle annular dark-field scanning transmission electron microscopy analysis, which provided practical structural modes for the SP-WSe_2. Note in Figure 1d that the major reflection can be indexed with the P63/mmc corresponding to WSe_2, in good agreement with JCPDS No. 87–2418 (Figure 1d). HRTEM image of a focus ion beam cut at the top region (Figure S2, Supporting Information) presents the detailed structure of the SP-WSe_2, verifying that the atoms are in the octahedral symmetry with trigonal prismatic coordination in 1T phase. Within the sandwich-like structure, the W atom in WSe_2 unit coordinates with six adjacent Se atoms to form a distorted octahedron, which buckles the layer of Se atom. A van der Waals stack of layers in ABA sequence finally composes the observed 1T phase bulk crystal structure. Significantly, the particular linkages between W and Se are expected to play a key role in the efficient transport of carriers.[27]

The SP-WSe_2, consisting of highly electronegative W^{4+} cations in the array structure that can be reduced during K-ions insertion, calls for an assessment of its electrochemical performances. With potassium metal as counter electrodes and 1 M KPF_6 in EC+DEC (v/v = 1:1) as the electrolyte, the K-ion half-cell (KIB) was first assembled in Ar-filled glove box. Figure 1f shows the typical cyclic voltammetry (CV) profiles of SP-WSe_2 at a scan rate of 0.2 mV s^{-1} in the voltage range of 0.01–3.0 V. It identifies two pairs of noticeable reduction and oxidation peaks around 1.3 and 1.6 V, respectively, which are associated with the reversible insertion of K-ions inside the WSe_2 layer and conversion of W^0/W^{4+}. The galvanostatic discharge/charge (GDC) curves of SP-WSe_2 at 0.1 A g^{-1} exhibit two voltage plateaus, which are well-matched with the CV curve. Figure 1h shows the cycling performance of the SP-WSe_2 anode at 1 A g^{-1}. Although the SP-WSe_2 delivers high capacities during the initial stage of the cycles, the capacities declined rapidly to 180 and 95 mAh g^{-1} after 20th and 100th cycles, respectively (Figure 1h), which can be further verified by the rate performance (Figure S3, Supporting Information). After analyzing the discharge profiles from 2nd to 100th cycles, we carried out SEM measurements of the SP-WSe_2 anode after 2nd, 20th, and 50th cycles (**Figure 2**a and Figure S4, Supporting Information). Notably, the degree of structural breaking to the material is positively correlated with the number of cycles, an observation that may ascribe to the irreversible lattice fracture causes active material dissolution. To circumvent the issues, an urgent that needs to reveal, to begin with, is the electrochemical and capacity-deterioration mechanisms of the SP-WSe_2 anode material.

2.2. Reaction and Capacity-Degradation Mechanism of the WSe_2 System

The in situ XRD results in Figure 2b show that, apart from the peak shifting, asymmetric peak evolutions were clearly observed during the cycling, demonstrating a two-phase reaction. Strikingly, in the region of discharge, with the voltage slope from open circuit voltage (OCV) to 0.01 V, the peak at

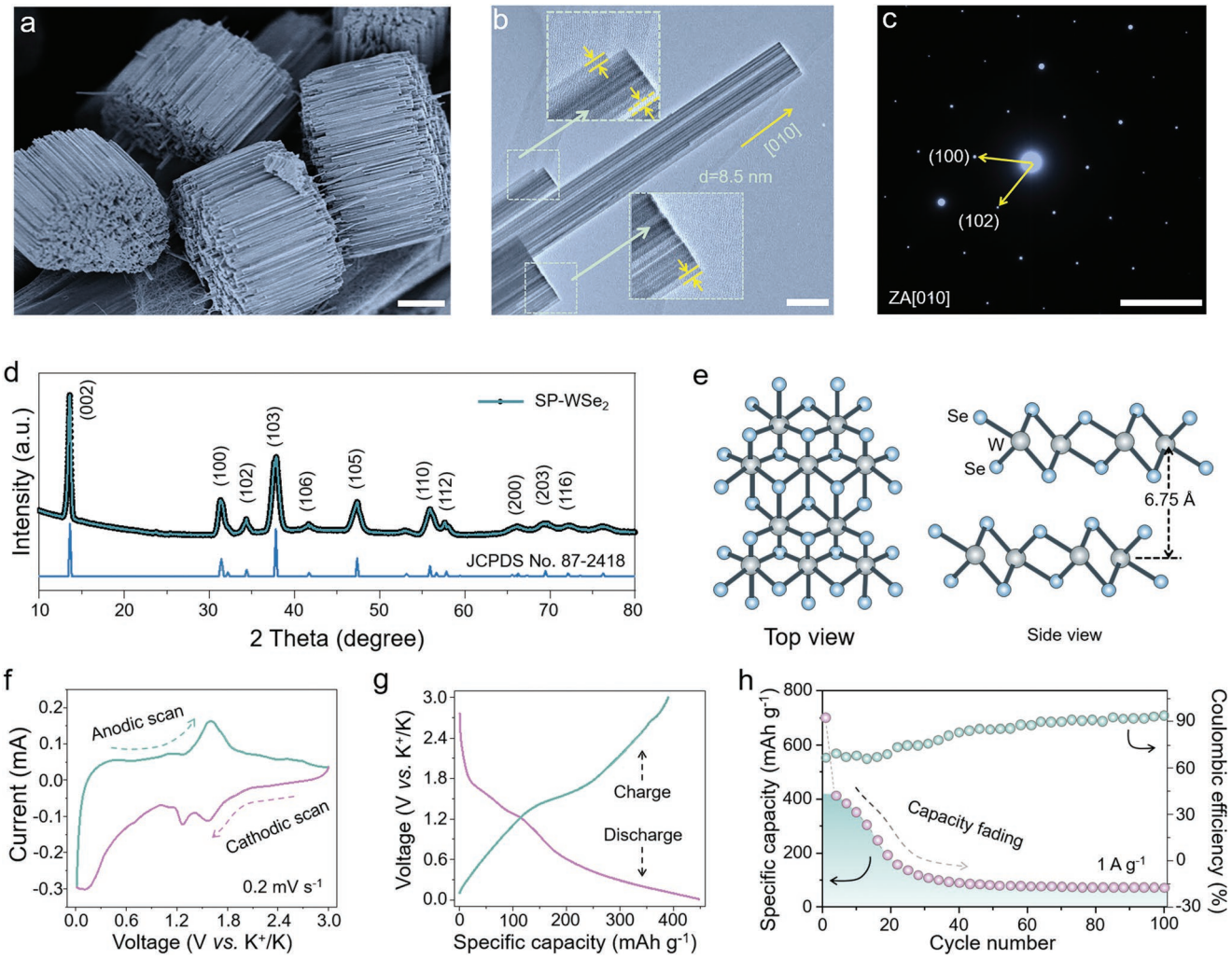

Figure 1. Structural and electrochemical characterization of the SP-WSe_2. a) The typical SEM image, b) HRTEM images, c) SAED pattern, d) XRD pattern, and e) Schematic structure of the SP-WSe_2. f) Cyclic voltammetry curves, g) Typical galvanostatic discharge/charge curve at 0.1 A g^{-1} between 0.01 and 3.0 V of the KIB. h) Cycling performance at 1 A g^{-1}. Scale bars, 2 µm (a), 200 nm (b), 5 1/nm (c).

ca. 41° shifted to a lower angle with increasing *d*-spacing for WSe_2. The initial (002) peak disappeared and another two new peaks assigned to K_2Se appeared at ca. 10° and 55° after the discharge process, indicating a sufficient conversion of WSe_2.[19] However, the difference from the other TMDs electrodes is that K_2Se can still be detected after fully depotassiation, indicating that the K-ion storage in WSe_2 is a partially reversible or irreversible conversion process that cannot be identified by XRD measurement. For further examination of this issue, ex situ XPS was carried out on the SP-WSe_2 at different electrochemical states (Figure 2c,d). To avoid any reaction between the trapped electrolyte and moisture during the measurements, the electrodes were washed with propylene carbonate and ethanol under an argon atmosphere, and finally collected via filtration. It reveals the presence of metallic W° following potassiation. However, the W^0 is not fully oxidized after being fully charged and the fraction of W^0 is ca. 41% (Figure S5, Supporting Information), indicating that the conversion reaction of the SP-WSe_2 is partially reversible. This is different from previous reports, where WSe_2-based electrodes undergo reversible conversion reaction during the cycling, regarded as a mixture of W^0 and LiSe/NaSe when discharged to 0.01 V, which is attributed to the larger ionic radii of K-ions and hence more sluggish reaction kinetics as compared with Li and Na-ions.[28–30]

The ex situ HRTEM measurements (Figure S6, Supporting Information) permit direct visualization of the partially reversible K-ion intercalation process in the SP-WSe_2. The reaction begins at the OCV (1.78 V) versus K^+/K with all the lattice fringes indexed to the WSe_2. As potassiation proceeds, the ex situ HRTEM images show that the lattice spacing increases (Figure S6b, Supporting Information) owing to the insertion of K-ions to form K_xWSe_2, agreeing well with the results of in situ XRD (Figure 2a). At fully discharged to 0.01 V, the crystallographic plane of the electrode increases (Figure S6c, Supporting Information) with the phase segregation of W, K_2Se, and K_xWSe_2, confirming that a part of the conversion reaction occurs. When fully charged to 2.97 V, the lattice spacing is partially recovered, resulting in the extraction of K-ions from the electrode. According to a systematic analysis based on in situ XRD, ex situ XPS, and ex situ HRTEM, the energy storage

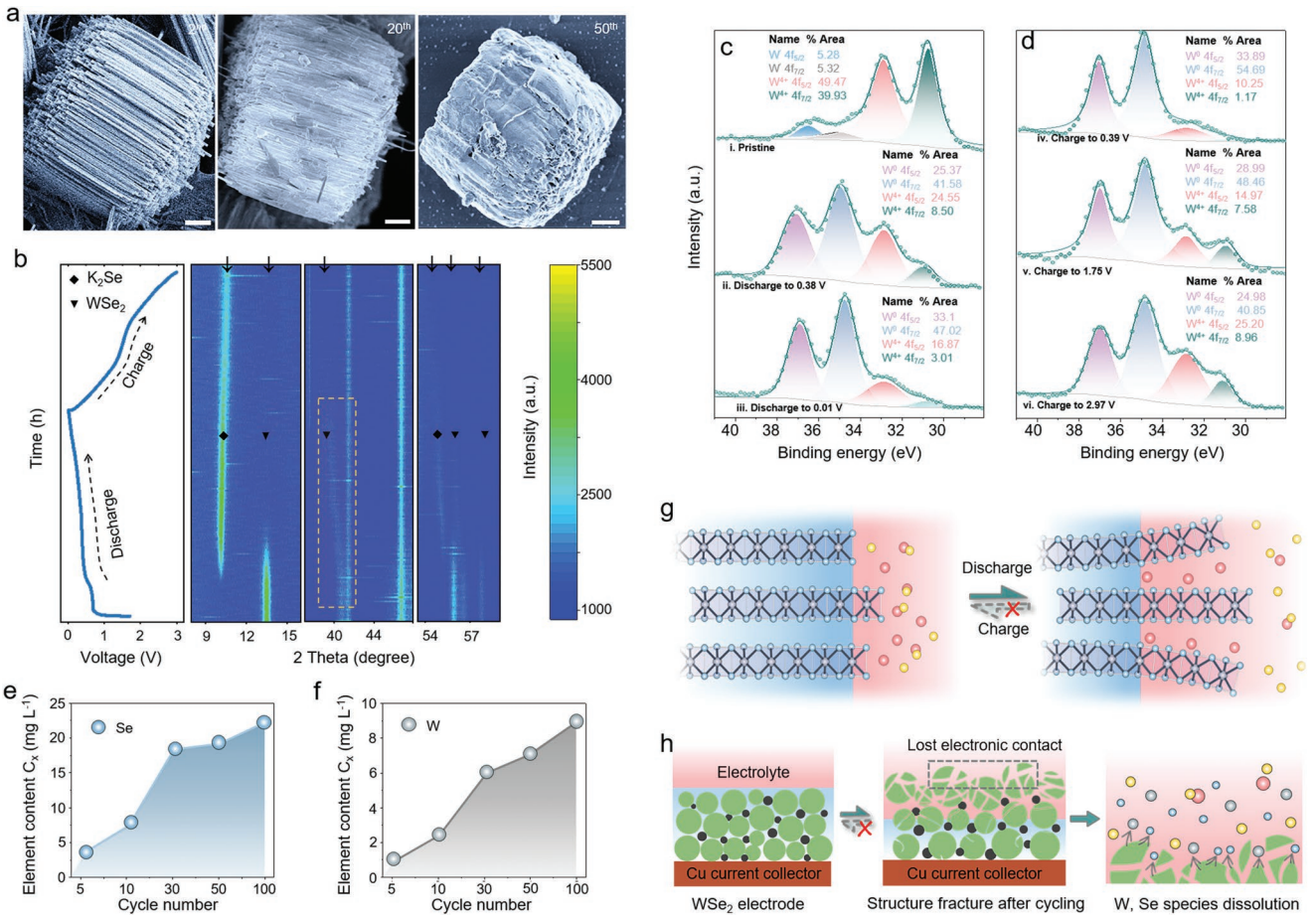

Figure 2. Observation of the phase transformation and the capacity-degradation of the WSe_2 system. a) Ex situ FESEM images of the SP-WSe_2 as anode after 2nd, 20th, and 50th cycles at 0.1 A g^{-1}. b) The initial discharge/charge profiles of the SP-WSe_2 and the corresponding in situ XRD patterns showing the evolution of Bragg reflections of WSe_2. Ex situ XPS W 4*f* spectra of an SP-WSe_2 anode during the c) discharging and d) charging process. e,f) AAS-determined W and Se species concentration of the electrolyte of the KIBs containing an SP-WSe_2 anode after different cycles. g,h) Schematic illustration of the proposed capacity-deterioration mechanisms for the SP-WSe_2 anode. (K in red, W in gray, Se in blue, conductive black in black, PF_6^- in yellow). Scale bars, 1 µm (a).

behavior of WSe_2-based anode during discharge/charge cycles can be tentatively proposed as follow:

Intercalation stage:

$$xK^+ + xe^- + WSe_2 \leftrightarrow K_xWSe_2 \quad (1)$$

Partial conversion stage:

$$K_xWSe_2 \leftrightarrow K_2Se + W \quad (2)$$

To explore the capacity fading mechanism and decisively associate it with the effective modification of the WSe_2 system, we collected the atomic absorption spectra of W and Se in electrolytes at different cycles. From the 0th cycle to the 100th cycle, the amounts of W and Se species increase significantly, revealing the migration of active W and Se species from the WSe_2 electrode to the electrolyte upon discharge/charge cycling (Figure 2e,f). The SP-WSe_2 anode underwent serious structural pulverization upon long cycling, while the intensity of the W signals decreased progressively with the stage of potassiation. This process is similar to the loss of polysulfides from the sulfur cathode observed for Li-S batteries.[31] As schematized in Figure 2g,2h, the capacity fading of the WSe_2-based electrode can be attributed to the following two reasons: 1) The limited diffusion path and large ionic radii of K-ion restrict the reversible (de)insertion and diffusion of K-ions into host lattice and generating huge expansion of the active material, resulting in a sluggish rate capability and poor cyclic stability; 2) The gradual migration of W and Se species from the anode to the electrolyte, resulting in a loss of the active material.

2.3. Structure and Performance of Designed the SP-K_xWSe_2 Anode

Based on the above capacity-deterioration mechanism, we proposed a facile pre-insertion strategy of K-ions in WSe_2 interlayer with a self-optimizing function for protecting the SP-WSe_2 anode. The synthesis procedure of SP-K_xWSe_2 is illustrated through the "pre-potassiation" strategy (**Figure 3**a) and the more detailed synthesis strategy is shown in the Experiment Methods (Supporting Information). The synthesized SP-K_xWSe_2 has a

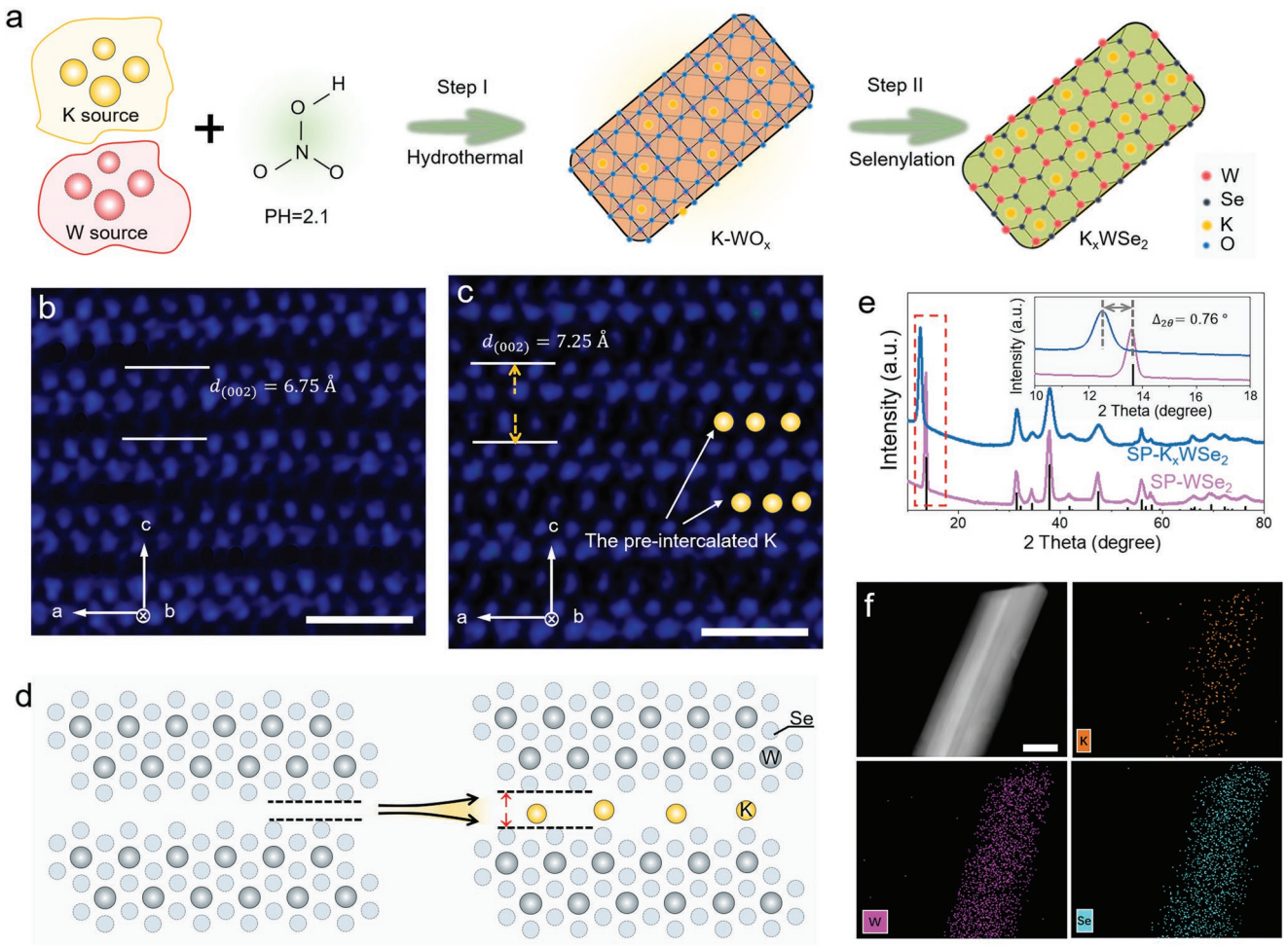

Figure 3. Demonstration of structure optimization. a) Schematic illustration of K_xWSe_2 synthesis. The HRTEM images of the b) SP-WSe_2 nanorod and the c) SP-K_xWSe_2 nanorod. d) Structural evolutions of WSe_2 during the "hydrothermal potassiation" process. e) XRD patterns. f) EDS mapping of the SP-K_xWSe_2. Scale bars, 1 nm (b and c), 50 nm (f).

typical crystalline microstructure with bundle secondary particles, which consist of smooth-faced primary nanorods (median diameter is ca. 10 nm; Figure S7, Supporting Information). The K-ion, which partially occupies the interlayer site, is expected to act as interlayer pillar and expand the interlayer structure to achieve the rapid K-ion diffusion coefficient in K_xWSe_2. The HRTEM images in Figure 3b show the interlayer channel surrounded by two atomic columns (blue spheres) corresponding to the channel walls on each side. Obviously, the interlayer channels of K_xWSe_2 are decorated with potassium atomic columns around their central positions (yellow spheres), based on which the atomic model along [002] is provided in Figure 3d. It can also be seen that SP-WSe_2 were successfully potassiation during hydrothermal because surplus K-ions were placed in a solution to support the expanded interlayer channels during their initial formation (Figure 3c,d).

The structural analysis of the SP-WSe_2 after hydrothermal treatment is performed using XRD and energy-dispersive spectroscopy (EDS). Figure 3e shows that the SP-K_xWSe_2 phase is well maintained after the hydrothermal treatment without new peak generation. However, after the hydrothermal treatment, the (002) peaks shift towards lower angels and the trend can be clearly observed by the insert image (Figure 3e), associated with the slightly improved interlayer spacing from 6.75 Å for SP-WSe_2 to 7.25 Å for SP-K_xWSe_2. Moreover, EDS mapping along the [010] direction shows a homogeneous distribution of K, W, and Se in the well-defined nanorod bundles (Figure 3f). Based on the weight fractions of K, W, and Se elements in the as-synthesized sample (Figure S8, Supporting Information), the atomic ratio of K/W for SP-K_xWSe_2 was calculated to be ca. 0.21.

Attributing to the presence of interlayer cations optimizes both the K-ion diffusion kinetics and structural stability of SP-K_xWSe_2, the rate capability of the KIB would be supposed to be improved when K-ions occupy the interlayer tunnels. Surprisingly, the CV curves of SP-K_xWSe_2 show higher peak potential and current density due to its excellent dynamics and high polar nature that leads to high electrical conductivity. The overlapping of 1st to 3rd curves, which is different from SP-WSe_2, indicates the good cyclic stability of the SP-K_xWSe_2 anode (**Figure 4**a). Moreover, to visualize the effects of pre-intercalated K-ion on cyclic stability, the rate capability of SP-K_xWSe_2 anode is shown in Figure 4b. The SP-K_xWSe_2 exhibits superior rate

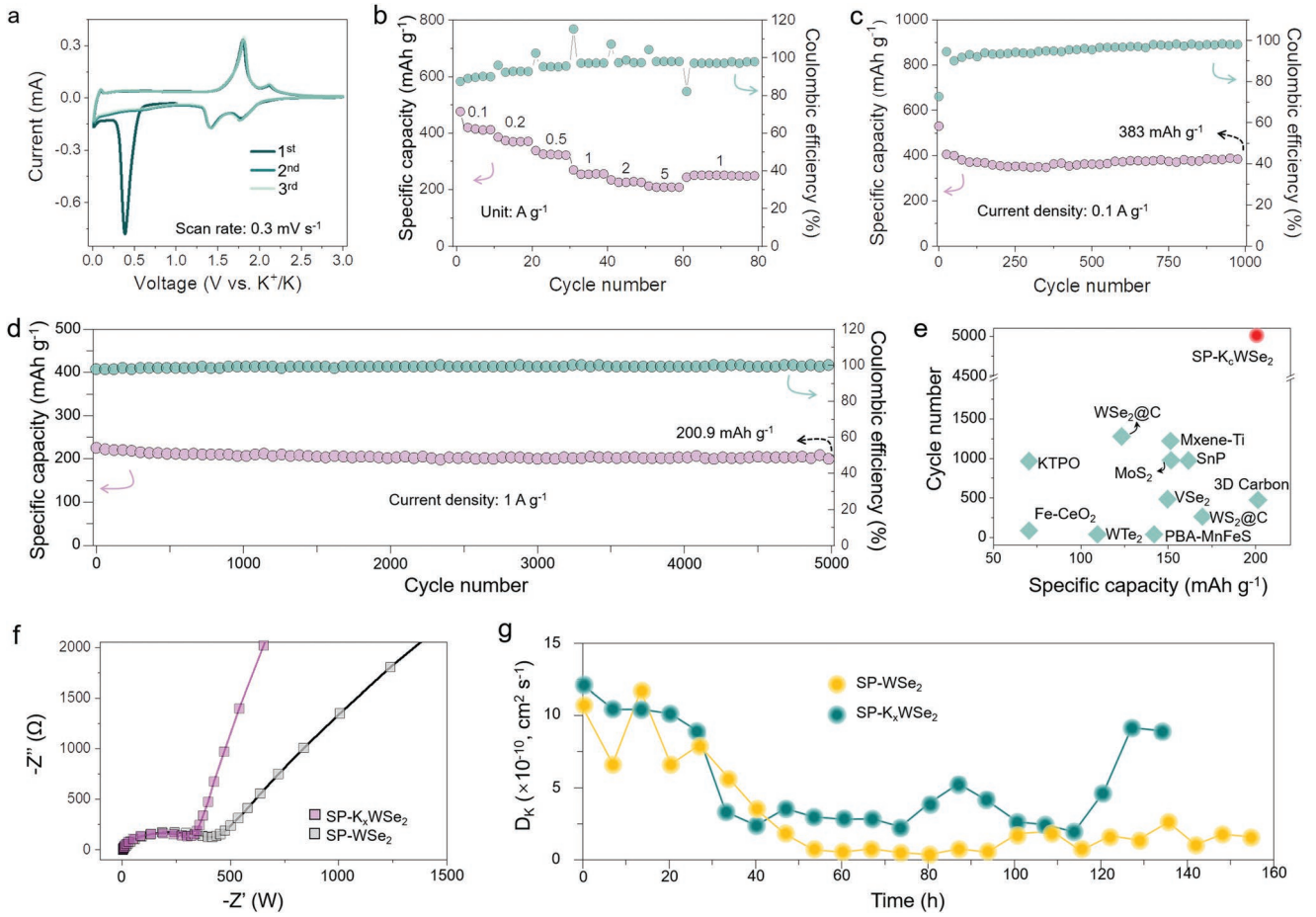

Figure 4. Electrochemical analysis and conductivity measurements of the SP-K_xWSe_2 anode in KIBs. a) CV curves at a scan rate of 0.3 mV s^{-1}. b) Rate capabilities at different current densities. Long-term cycle performance at c) 0.1 and d) 1 A g^{-1}. e) The comparison of specific capacity versus cycle number of the SP-K_xWSe_2 anode with various reported research electrodes for KIBs. f) Impedance spectra (Nyquist plots) of the SP-K_xWSe_2 and SP-WSe_2 anodes. g) The calculated chemical diffusion coefficient for K-ion in the SP-K_xWSe_2 and SP-WSe_2 anodes versus cycle time.

capability compared with SP-WSe_2, especially under high current density. High reversible capacities of 418, 384, 319, 257, and 225 mAh g^{-1} were delivered at 0.1, 0.2, 0.5, 1, and 2 A g^{-1}, respectively. Even at a high current of 5 A g^{-1}, a stable reversible capacity of 211 mAh g^{-1} was still maintained. This value is approximately seven times higher than that of SP-WSe_2. When the current density is switched abruptly from 5 to 1 A g^{-1} again, the discharge capacity can be recovered to its initial value without any sign of capacity loss.

In addition to its superior rate capability, SP-K_xWSe_2 also displays high cycling stability (Figure 4c,d). It provides a reversible capability of 401.2 mAh g^{-1} and excellent cycling stability with 95.5% capacity retained after 1000 cycles at 0.1 A g^{-1}. Furthermore, at a large specific current of 1 A g^{-1}, the activated SP-K_xWSe_2 can deliver a reversible capacity of 200.9 mAh g^{-1} with a capacity retention of 89.3% even after 5000 cycles, with only 0.0021% capacity decay per cycle. We have also compared the performance parameter with state-of-art representatively reported congeneric KIBs such as MoS_2/C//K, C-WS_2@CNF//K, VSe_2//K, WSe_2//K, Td-WTe_2//K, Mn-Fe-Se/CNT//K, Sn_4P_3//K, TiO_xN/C//K, $KTi_2(PO_4)_3$@C//K, Fe-CeO_2//K, and 3D N-C//K in Figure 4e and Table S1, Supporting Information.[7,19,32–40] In general, in contrast to the low cycling stability and low specific capacity at moderate current densities observed in typical KIBs, SP-K_xWSe_2 exhibits outstanding electrochemical performances, attributed to the advantage of the optimized structure resulting from the introduction of K-ions.

To understand the possible (de)potassiation mechanism of K_xWSe_2, the in situ XRD and ex situ XPS were carried out during the first discharge/charge cycle at 0.025 A g^{-1}. Figure S9, Supporting Information, shows the in situ XRD results for K_xWSe_2 at different potassiation states. When the K_xWSe_2 electrode is discharged to 0.75 V, the (002) peak shifts to the lower angles with increasing *d*-spacing for K_xWSe_2. After the electrode is further fully discharged to 0.01 V, the peaks of K_xWSe_2 are missing, and the diffraction peaks of K_2Se are found at 9.76° and 34.7°. Being different from the SP-WSe_2, as the depotassiation continues, the peak of K_xWSe_2 starts to recover while the intensity of K_2Se peaks gradually decreases, indicating a highly reversible structure evolution of the K_xWSe_2 during the continuation of conversion reactions. These results were further verified by ex situ XPS measurements (Figure S10 and Figure S11, Supporting Information). The valence change of W in different potassiation states of K_xWSe_2 is similar to

that of SP-WSe_2. However, one of the most important differences in K_xWSe_2 is that the relative content of residual W in the fully charged electrode is much less than that of SP-WSe_2, which indicates that the electrochemical reversibility of K_xWSe_2 is greatly enhanced during cycling. Shown in Figure S12, Supporting Information, is the SEM images of the K_xWSe_2 after 0, 20, and 50 cycles at 0.1 A g^{-1}, yet keeping other experimental variables fixed. Microstructural characterization of the morphology shows that the K_xWSe_2 exhibit negligible changes on both the surface and the volume, corroborating the high structural stability during cycling.

It is of great interest to study the dependence of pre-potassiation efficiency on the material structure, the micron-sized WSe_2 bulk (b-WSe_2) material was synthesized under different synthesis conditions of the SP-WSe_2, and the details are shown in Experiment Methods. As observed via FESEM (Figure S13a,b, Supporting Information), the b-WSe_2 materials are loosely agglomerated and have a mean particle size of 200–500 µm. With the same pre-potassiation treatment, the K content in the obtained pre-intercalated b-WSe_2 (b-K_xWSe_2) is different. The corresponding EDS elemental mappings of K, W, and Se elements for b-WSe_2 and b-K_xWSe_2 are shown in Figure S14, Supporting Information. It is seen that W and Se are uniformly distributed in the whole material while the atomic dots of K are barely detectable, implying the K ions cannot intercalate inside the bulk during "pre-potassiation". The overall atomic ratio of K was calculated to be around 0.08 by EDS, which is close to the b-WSe_2 sample (Figure S15, Supporting Information). Figure S16, Supporting Information, shows the rate capabilities and cycling performances of the b-WSe_2 and b-K_xWSe_2 anode. Although the b-K_xWSe_2 delivered larger capacities during the early stage of the cycles, its capacity decreased as rapidly as the b-WSe_2. Therefore, a nanoarray structure with reduced K-ion diffusion length and large surface area is crucial for successful K-ion intercalation and improved performance of WSe_2-based materials.

2.4. Effect of K-Ions on Electronic and Ionic Conductivities

The origin of the superior K-ion storage presented in the SP-K_xWSe_2 anode was further evaluated by thermodynamics and kinetics studies based on electrochemical impedance spectroscopy (EIS) and galvanostatic intermittent titration technique (GITT) measurements. The impedance spectra (Nyquist plots) of KIBs with SP-K_xWSe_2 and SP-WSe_2 as the active material before electrochemical tests have been collected (Figure 4f). The resultant EIS spectra have been fitted according to the Randles equivalent circuit, consisting of high-frequency depressed semicircles and low-frequency linear tails, in which the former is related to the surface resistance (R_{sf}), and the latter is ascribed to the charge transfer resistance (R_{ct}).[41] It is evident that the R_{ct} of the anode decreases as the K-ions intercalated in the layered structure. The steeper line at low-frequency region for the SP-K_xWSe_2 also certifies the improved electrical conductivity of the sample with the introduction of K-ions.

The quasi-equilibrium open-circuit-voltage and transient voltage response of the assembled KIBs during the electrochemical tests were measured by GITT (Figure S17, Supporting Information). The GITT tests were conducted after 3 cycles of the fresh KIBs at 0.025 A g^{-1}, in which the cells were alternately discharged for 10 min followed by 90 min resting, then charged in the same way. Figure S18a, Supporting Information, displays two GITT steps of the SP-WSe_2 anode in terms of the discharge. It is evident that the E displays an approximately linear relation with $t^{1/2}$ (Figure S18b, Supporting Information). To prob the ionic and electronic transport properties of the SP-K_xWSe_2 anodes, we determined the reaction resistance (R_r, calculated by dividing the overpotential by the pulse current density) from the GITT and compared it with the SP-WSe_2 anode (Figure S19, Supporting Information).[42] In the process of potassiation, R_r of the SP-K_xWSe_2 experiences a slow increase after the voltage reaches 1. 5 V, and then displays a negative correlation characteristic as the depth discharge progresses. In contrast, the R_r of the SP-WSe_2 anode exhibits an obvious increase (12.5 Ω g) during electrochemical measurements, which is much larger than the 7 Ω g of the SP-K_xWSe_2, implying that sluggish K-ion kinetics may occur in the SP-WSe_2 anode. The calculated K^+ diffusion co-efficient (D_{K^+}) during (de)potassiation is shown in Figure 4g. The D_{K^+} of SP-WSe_2 and SP-K_xWSe_2 samples are close due to both open-layered structures but D_{K^+} of SP-K_xWSe_2 is higher, which can ascribe to larger interlayer diffusion channels. The comparison of electronic and ionic conductivities of SP-WSe_2 and SP-K_xWSe_2 samples are displayed in **Table 1**. The enhanced electrochemical performance of K_xWSe_2 is attributed to the improved K^+ diffusion coefficient and electrical conductivity via pre-intercalated K^+ ions. Therefore, more pronounced redox peaks and superior rate capability and cycling stability can be achieved (Figure 4a–d).

We reveal the fundamental mechanism of the fast while reversible K-ions storage in the microstructure of K_xWSe_2 and prove the experimental results above using density functional theory (DFT) calculations, wherein the calculations were carried out based on a periodic $5 \times 4 \times 2$ supercell of WSe_2. It can be inferred that the hexagonal (H) site and tetrahedral (T) site are available for K storage, denoted as H and T, respectively (**Figure 5**a,b). The lower total energy and bigger layer spacing (shown in Figure 5c,d) indicate that H sites are energetically favorable compared to T sites upon the "pre-potassiation" process. It is interesting to note that the K is embedded in H site (K_H) has a more obvious effect on the expansion of layer spacing, as indicated by the spacing changing from 7.47 Å for the K_HWSe_2 to 7.31 Å for the K_TWSe_2 in Figure 5c,d. The simulated lattice constants and formation energy of K intercalating into the supercell are provided in Tables S2 and S3, Supporting Information. We further investigated the K-ion diffusion in the interlayer of K_HWSe_2 layers (Figure 4e–g). It is notable that much lower diffusion energy barriers for K-ion diffusion in the K_HWSe_2 (Figure 5g) were obtained than those on WSe_2. The charge transfers upon intercalation are investigated based

Table 1. Transport properties derived from the impedance spectra (at $T = 25$ °C).

Sample	R_{sf} [Ω]	R_{ct} [Ω]	R_r [Ω g]	D_K [cm^{-2} s^{-1}]
SP-WSe_2	5.36	442.4	9.98	3.95×10^{-10}
SP-K_xWSe_2	6.98	329.2	6.01	3.73×10^{-9}

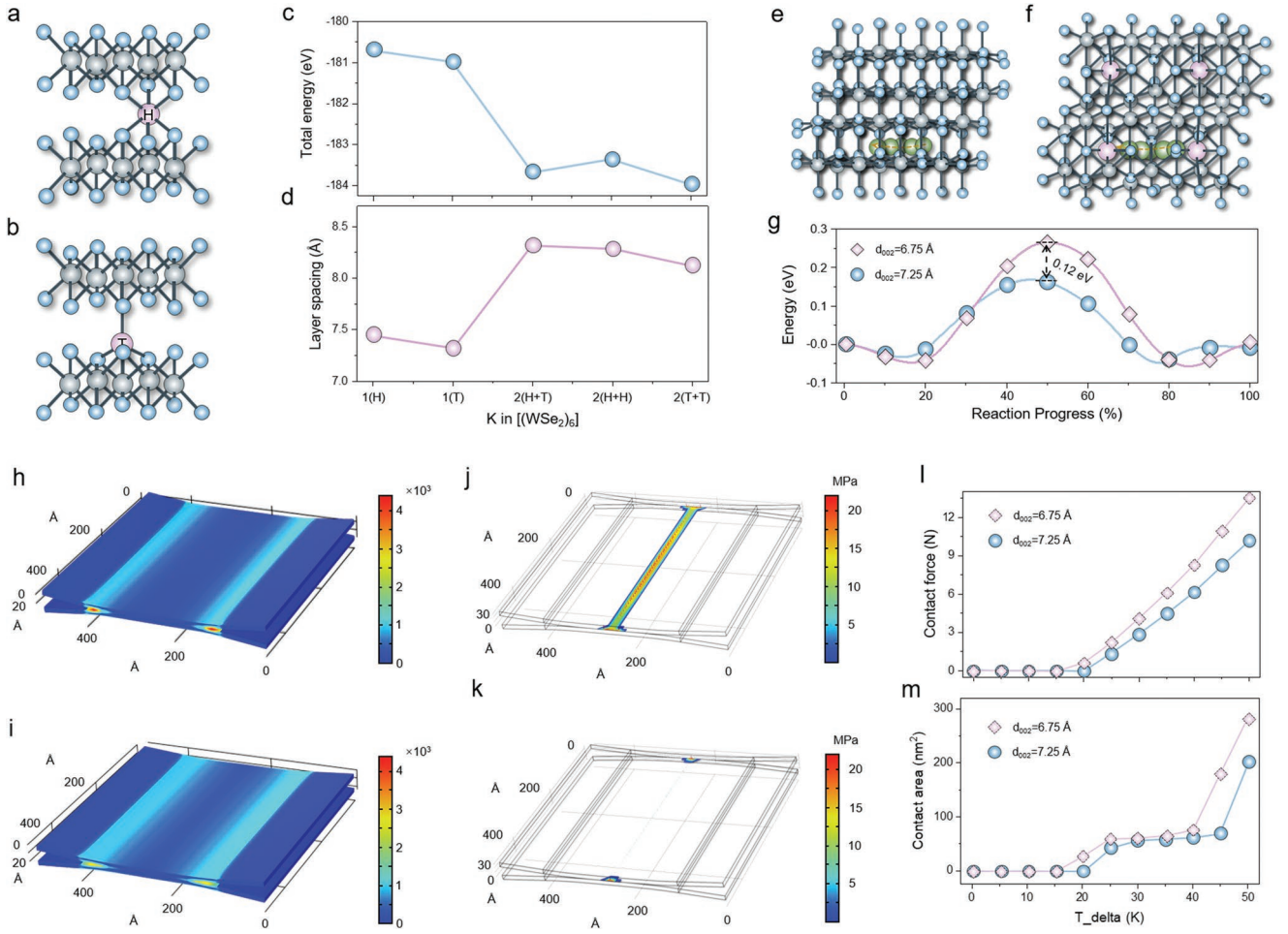

Figure 5. K-ion insertion effects on structural and reactions. a,b) Two stable adsorption sites for K-ions in the WSe_2 bilayer. c) Total energies and d) layer spacing of the supercell after the insertion of K-ions. Selected diffusion pathway of K-ions in e) SP-WSe_2, f) SP-K_xWSe_2, and g) the corresponding calculated diffusion barriers. h) Stress and j) strain distribution caused by the internal expansion of WSe_2. i) Stress and k) strain distribution caused by the internal expansion of K_xWSe_2. The corresponding l) contact force and m) sectional distributions of the external applied vertical Von-Mise stress on two-layered WSe_2-WSe_2 units in thermodynamic temperature range of 0 to 50 K.

on the corresponding charge-density difference (Figure S20, Supporting Information). K-ion in K_HWSe_2 loses its electron to adjacent selenium atoms (Se) and the transferred charge is highly localized, resulting in a similar capacitive behavior as that in $NbSe_2$ material. Obviously, the values were sufficiently low to enable fast K-ion diffusion within K_HWSe_2 at room temperature. Even if our DFT calculations were unable to simulate the detailed conversion reaction, they did provide some computational support to the remarkable electrochemical performance observed experimentally.

The underlying enhancement mechanism for reversible redox chemistry is evaluated using the density of states, as calculated by DFT at different states (Figure S21, Supporting Information). For the initial state, the Mott–Hubbard splitting, precisely, the d-d Coulombic interaction term U, is smaller in the K_xWSe_2 sample attributed to the K-ion in the interlayer and the structural distortion caused by it. The fact is, U is inversely proportional to the orbital volume, a larger radius of $W^{(4-x)+}$ relative to W^{4+} will also lead to a smaller U. Then, in the completely depotassiated state, the Se-K-Se band in K_xWSe_2 is more likely to be a reversible damaged. Furthermore, in terms of qualitative analysis, assuming that the W ions in both samples are reduced to W^0, both the smaller radius and the half-filled t_{2g}^3 state lead to a decrease in U. In this state, electrons are easily removed from the K *2p* non-bonding band, which can also be confirmed in Figure S21, Supporting Information. In comparison, the irreversible structural damage prevents the decrease in term U for the WSe_2 sample. Furthermore, the simulation results indicate that the reduced d-band width and d-band center are closer to the Fermi level, which is due to the fact that the insertion of K favors the tuning of U.

To explore the mechanical properties of SP-WSe_2 and SP-K_xWSe_2, the finite element analysis was performed to simulate the effort of pre-intercalated K-ion on structural change by thermal expansion process. For an approximate simulation, the two restacked bilayer structures were employed to analyze the internal self-extrusion process. The two sides are fixed as constraint conditions according to the experimental results, and the maximum value is marked in the corresponding position with black dot. Note that the specific value is calculated from

the thermodynamic process only for comparison. It can be clearly seen that the insertion of K-ions from both sides leads to a scissor-like deformation of the rigid structure, where the stress rises significantly in the central part (Figures S22 and S23, Supporting Information). The stress and deformation degree of the restacked bilayer structure with larger interlayer spacing is smaller, proving the superiority of expanded layer spacing in 2D multilayered structures (Figure 5h,i). Moreover, we further investigated the distribution of external Von-Mise stress on restacked WSe_2 bilayers surface (Figures S24 and S25, Supporting Information). As shown in Figure 5j,k, the stress on the surface of K_xWSe_2 is more even and the peak value is smaller. It is notable that the layered WSe_2 structure undertakes higher stress and larger deformation degree due to the higher expansion coefficient and lower Young's modulus of WSe_2, which are well confirmed by the direct ex situ SEM observation of the electrodes. On account of the extremely poor mechanical strength and large volume expansion of WSe_2, the layered structures were completely destroyed soon after cycling, leading to a low Coulombic efficiency and rapid capacity decay.[43] Apparently, owning to the optimized structure with larger layer spacing, the K_xWSe_2 subunits with high Young's modulus show effective enhancement compared to WSe_2, as shown in contact force and sectional distributions result in Figure 5l,m and Figure S26, Supporting Information. And the large interlayer spacing subunit can guarantee the integrity of the layered material, which makes it possible for the protection of fragile metal selenides to cycle for a long time.

2.5. Assembling a KIHC

Considering that the SP-K_xWSe_2 possesses rapid K-ion diffusion kinetic and excellent long-term stability, KIHCs were assembled in typical coin cell configurations, where the prepared SP-K_xWSe_2 was employed as negative materials for the (de)insertion of K-ions (**Figure 6**a). Activated carbon (AC) derived from peanut shells is an ideal capacitive type cathode material since it possesses a hierarchical porosity and high specific surface area (Figure S27, Supporting Information), guaranteeing the rapid (de)adsorption of K^+.[44] The KIHCs skillfully combine the electrochemical mechanisms of both the electronic double-layer capacitor (EDLC) and KIBs, and bridging the properties of them with superior rate capability and capacitance, which is distinctly distinguished from the conventional EDLC. Upon discharging, K-ions are inserted into SP-K_xWSe_2 (Faradaic reaction), while the PF_6^- anions are absorbed on the electrode-electrolyte interface (non-Faradaic reaction). Here, the charge balance ($q^+ = q^-$) between the electrodes was achieved by adjusting the mass loading of the SP-K_xWSe_2 and AC.[45,46] The electrochemical performances of the assembled SP-K_xWSe_2//AC KIHCs were performed by CV

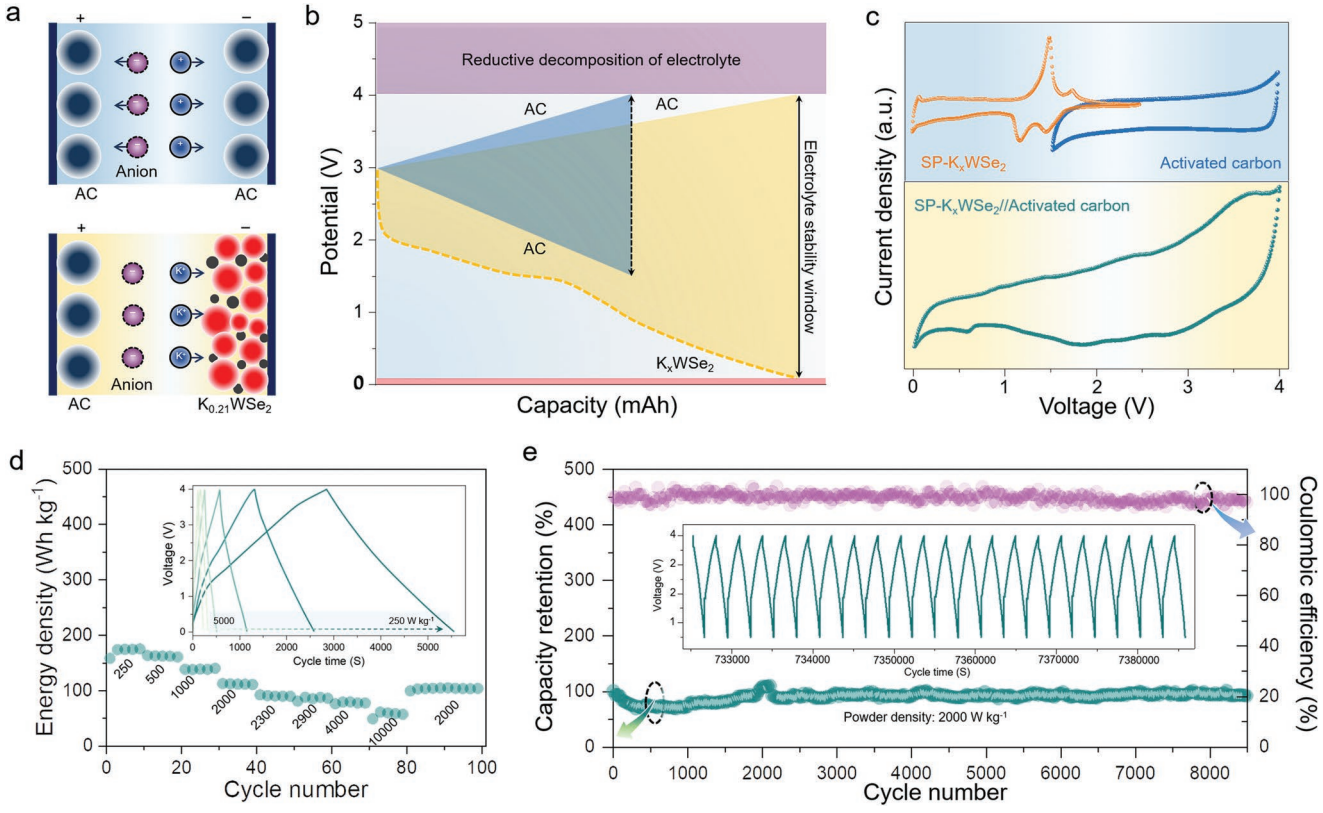

Figure 6. Electrochemical performance of the SP-K_xWSe_2//AC KIHCs. a) Schematic of energy storage mechanisms of typical EDLC and KIHC. b) Voltage profile of EDLC and novel KIHCs. c) CV curves of the SP-K_xWSe_2 and the AC electrodes in KIBs (top) and full cell of KIHCs (bottom) at fixed 0.3 mV s^{-1}. d) Rate capability of the KIHCs. The inset shows the GDC voltage profiles at different power densities between 250 and 10 000 W kg^{-1}. e) Cycle performance and Coulombic efficiency for 8500 cycles at a power density of 2000 W kg^{-1}.

and GDC measurements. The slight distortion from the ideal rectangular CV curve and approximately linear GDC profile of the SP-K_xWSe_2//AC KIHCs indicate a multiple charge storage mechanism of faradaic and non-faradaic reactions in both electrodes (Figure 6c,d). Besides, the GDC curves of the KIHC at different power densities varying from 250 to 10 000 W kg^{-1} in the voltage range between 0.01–4.0 V is shown in Figure 6d. As expected, a maximum energy density of 175 Wh Kg^{-1} could be achieved at a power density of 250 W Kg^{-1}, maintaining above 63 Wh Kg^{-1} even at 10 000 W Kg^{-1}, indicating the sustainable high current endurance of the SP-K_xWSe_2 based KIHCs (Figure 6d). Furthermore, the SP-K_xWSe_2//AC KIHC is very stable as it maintains over 94.8% of its initial capacity with nearly 100% Coulombic efficiency over 8500 cycles at a high power density of 2000 W kg^{-1}, corresponding to only 0.0006% fading per cycle (Figure 6e). The radar charts summarize the six figure-of-merits of the SP-K_xWSe_2//AC KIHC, including electrochemical window, energy density, power density, rate capability, cycle number, and capacity retention (Figure S28, Supporting Information). It clearly shows that the electrochemical performance of the assembled SP-K_xWSe_2//AC KIHC outperforms among KIHCs ever reported (detailed as shown in Table S4, Supporting Information).

3. Conclusion

In summary, K-ions pre-intercalated WSe_2 nanoarray structures were prepared via an effective "hydrothermal pre-potassiation" strategy, and investigated as the anode materials for potassium storage for the first time. The capacity-deterioration mechanism of an SP-WSe_2 anode was elucidated to be associated with the loss of W, Se species towards the electrolyte and the pulverization of WSe_2 upon repeated cycling. Subsequently, the introduction of K-ions was confirmed to prevent the loss of W and Se species towards the electrolyte while increasing the structural stability electronic conductivity, and K-ion diffusivity during repeated charge/discharge cycles. With fast K-ion diffusion kinetics and stable host structure, the prepared SP-K_xWSe_2 exhibit remarkable K-ion storage properties in KIBs and KIHCs that are superior to previous reports. The results of our comprehensive studies provide a valuable framework for the rational selection of channel cations to improve the rate performance of layer-based intercalation electrodes.

Supporting Information

Supporting Information is available from the Wiley Online Library or from the author.

Acknowledgements

X.Y. acknowledges the support from National Sciences Foundation of China (51971065) and the Innovation Program of Shanghai Municipal Education Commission (2019-01-07-00-07-E00028).

Conflict of Interest

The authors declare no conflict of interest.

Data Availability Statement

The data that support the findings of this study are available from the corresponding author upon reasonable request.

Keywords

capacity deterioration mechanism, K^+ pre-intercalated WSe_2, potassium-ion batteries, potassium-ion hybrid capacitor, ultrahigh stability

Received: September 4, 2022
Revised: October 23, 2022
Published online:

[1] M. Armand, J.-M. Tarascon, *Nature* **2008**, *451*, 652.
[2] M. Li, J. Lu, X. Ji, Y. Li, Y. Shao, Z. Chen, C. Zhong, K. Amine, *Nat. Rev. Mater.* **2020**, *5*, 276.
[3] Y. Jiang, Y. Yang, F. Ling, G. Lu, F. Huang, X. Tao, S. Wu, X. Cheng, F. Liu, D. Li, H. Yang, Y. Yao, P. Shi, Q. Chen, X. Rui, Y. Yu, *Adv. Mater.* **2022**, *34*, 2109439.
[4] Y. Zhu, X. Yang, D. Bao, X. Bie, T. Sun, S. Wang, Y. Jiang, X. Zhang, J. Yan, Q. Jiang, *Joule* **2018**, *2*, 736.
[5] H. Liang, Z. Gu, X. Zhao, J. Guo, J. Yang, W. Li, B. Li, Z. Liu, Z. Sun, J. Zhang, X. Wu, *Sci. Bull.* **2022**, *67*, 1581.
[6] W. C. Zhang, Y. J. Liu, Z. P. Guo, *Sci. Adv.* **2019**, *5*, eaav7412.
[7] S. Geng, T. Zhou, M. Jia, X. Shen, P. Gao, S. Tian, P. Zhou, B. Liu, J. Zhou, S. Zhuo, F. Li, *Energy Environ. Sci.* **2021**, *14*, 3184.
[8] P. Xiong, F. Zhang, X. Zhang, S. Wang, H. Liu, B. Sun, J. Zhang, Y. Sun, R. Ma, Y. Bando, C. Zhou, Z. Liu, T. Sasaki, G. Wang, *Nat. Commun.* **2020**, *11*, 3297.
[9] H. Liang, Z. Gu, X. Zheng, W. Li, L. Zhu, Z. Sun, Y. Meng, H. Yu, X. Hou, X. Wu, *J. Energy Chem.* **2021**, *59*, 589.
[10] H. Huang, J. Wang, X. Yang, R. Hu, J. Liu, L. Zhang, M. Zhu, *Angew. Chem., Int. Ed.* **2020**, *59*, 14504.
[11] C. Zhang, H. Zhao, Y. Lei, *Energy Environ. Mater.* **2020**, *3*, 105.
[12] R. Huang, J. Lin, J. Zhou, E. Fan, X. Zhang, R. Chen, F. Wu, L. Li, *Small* **2021**, *17*, 2007597.
[13] T. Hosaka, K. Kubota, A. S. Hameed, S. Komaba, *Chem. Rev.* **2020**, *120*, 6358.
[14] L. Fan, R. Ma, Q. Zhang, X. Jia, B. Lu, *Angew. Chem., Int. Ed.* **2019**, *58*, 10500.
[15] K. Zhang, Z. Gu, E. Ang, J. Guo, X. Wang, Y. Wang, X. Wu, *Mater. Today* **2022**, *54*, 189.
[16] Y. Fang, D. Luan, X. W. D. Lou, *Adv. Mater.* **2020**, *32*, 2002976.
[17] J. H. Choi, G. D. Park, Y. C. Kang, *Chem. Eng. J.* **2021**, 408.
[18] X. Chen, H. Muheiyati, X. Sun, P. Zhou, P. Wang, X. Ding, Y. Qian, L. Xu, *Small* **2022**, *18*, 2104363.
[19] L. Xing, K. Han, Q. Liu, Z. Liu, J. Chu, L. Zhang, X. Ma, Y. Bao, P. Li, W. Wang, *Energy Storage Mater.* **2021**, *36*, 309.
[20] B. Kang, X. Chen, L. Zeng, F. Luo, X. Li, L. Xu, M. Q. Yang, Q. Chen, M. Wei, Q. Qian, *J. Colloid Interface Sci.* **2020**, *574*, 217.
[21] Z. Zhang, M. Yang, N. Zhao, L. Wang, Y. Li, *Phys. Chem. Chem. Phys.* **2019**, *21*, 23441.
[22] Y. Yuan, C. Zhan, K. He, H. Chen, W. Yao, S. Sharifi-Asl, B. Song, Z. Yang, A. Nie, X. Luo, H. Wang, S. M. Wood, K. Amine,

M. S. Islam, J. Lu, R. Shahbazian-Yassar, *Nat. Commun.* **2016**, *7*, 13374.
[23] J. Huang, Z. Wang, M. Hou, X. Dong, Y. Liu, Y. Wang, Y. Xia, *Nat. Commun.* **2018**, *9*, 2906.
[24] A. Sood, A. D. Poletayev, D. A. Cogswell, P. M. Csernica, J. T. Mefford, D. Fraggedakis, M. F. Toney, A. M. Lindenberg, M. Z. Bazant, W. C. Chueh, *Nat. Rev. Mater.* **2021**, *6*, 847.
[25] B. Chen, D. Chao, E. Liu, M. Jaroniec, N. Zhao, S. Qiao, *Energy Environ. Sci.* **2020**, *13*, 1096.
[26] J.-H. Ha, P. Muralidharan, D. K. Kim, *J. Alloys Compd.* **2009**, *475*, 446.
[27] J. Sun, Y. Wang, S. Guo, B. Wan, L. Dong, Y. Gu, C. Song, C. Pan, Q. Zhang, L. Gu, F. Pan, J. Zhang, *Adv. Mater.* **2020**, *32*, 1906499.
[28] G. Zhang, X. Ou, J. Yang, Y. Tang, *Small Methods* **2021**, *5*, 2100374.
[29] P. Zhou, G. Collins, Z. Hens, K. M. Ryan, H. Geaney, S. Singh, *Nanoscale* **2020**, *12*, 22307.
[30] W. Yang, J. Wang, C. Si, Z. Peng, Z. Zhang, *Nano Res.* **2017**, *10*, 2584.
[31] J. Liang, Q. Sun, Y. Zhao, Y. Sun, C. Wang, W. Li, M. Li, D. Wang, X. Li, Y. Liu, K. Adair, R. Li, L. Zhang, R. Yang, S. Lu, H. Huang, X. Sun, *J. Mater. Chem. A* **2018**, *6*, 23712.
[32] B. Jia, Q. Yu, Y. Zhao, M. Qin, W. Wang, Z. Liu, C. Lao, Y. Liu, H. Wu, Z. Zhang, X. Qu, *Adv. Funct. Mater.* **2018**, *28*, 1803409.
[33] C. Yang, J. Feng, F. Lv, J. Zhou, C. Lin, K. Wang, Y. Zhang, Y. Yang, W. Wang, J. Li, S. Guo, *Adv. Mater.* **2018**, *30*, 1800036.
[34] D. M. Soares, G. Singh, *Nanotechnology* **2021**, *32*, 505402.
[35] J. Wang, B. Wang, X. Liu, J. Bai, H. Wang, G. Wang, *Chem. Eng. J.* **2020**, *382*, 123050.
[36] W. Zhang, W. K. Pang, V. Sencadas, Z. Guo, *Joule* **2018**, *2*, 1534.
[37] N. Wang, C. Chu, X. Xu, Y. Du, J. Yang, Z. Bai, S. Dou, *Adv. Energy Mater.* **2018**, *8*, 1801888.
[38] Z. Wei, D. Wang, M. Li, Y. Gao, C. Wang, G. Chen, F. Du, *Adv. Energy Mater.* **2018**, *8*, 1801102.
[39] Y. Ma, Y. Ma, H. Euchner, X. Liu, H. Zhang, B. Qin, D. Geiger, J. Biskupek, A. Carlsson, U. Kaiser, A. Groß, S. Indris, S. Passerini, D. Bresser, *ACS Energy Lett.* **2021**, *6*, 915.
[40] W. Zhang, J. Yin, M. Sun, W. Wang, C. Chen, M. Altunkaya, A. H. Emwas, Y. Han, U. Schwingenschlogl, H. N. Alshareef, *Adv. Mater.* **2020**, *32*, 2000732.
[41] N. Ding, J. Schnell, X. Li, X. Yin, Z. Liu, Y. Zong, *Chem. Eng. J.* **2021**, *412*, 128559.
[42] L. Deng, X. Niu, G. Ma, Z. Yang, L. Zeng, Y. Zhu, L. Guo, *Adv. Funct. Mater.* **2018**, *28*, 1800670.
[43] A. Falin, M. Holwill, H. Lv, W. Gan, J. Cheng, R. Zhang, D. Qian, M. R. Barnett, E. J. G. Santos, K. S. Novoselov, T. Tao, X. Wu, L. H. Li, *ACS Nano* **2021**, *15*, 2600.
[44] W. Qian, F. Sun, Y. Xu, L. Qiu, C. Liu, S. Wang, F. Yan, *Energy Environ. Sci.* **2014**, *7*, 379.
[45] L. Kong, C. Zhang, S. Zhang, J. Wang, R. Cai, C. Lv, W. Qiao, L. Ling, D. Long, *J. Mater. Chem. A* **2014**, *2*, 17962.
[46] J. Ding, H. Wang, Z. Li, K. Cui, D. Karpuzov, X. Tan, A. Kohandehghan, D. Mitlin, *Energy Environ. Sci.* **2015**, *8*, 941.